An Integral Battery Charger with Power Factor Correction for Electric Scooter.

Gianmario Pellegrino, Eric Armando and Paolo Guglielmi
Politecnico di Torino, Department of Electrical Engineering,
C.so Duca degli Abruzzi 24, 10129, Torino, Italy
Emails: (gianmario.pellegrino, eric.armando, paolo.guglielmi)@polito.it

ABSTRACT

An integral battery charger is proposed for an electric scooter with Li-Ion batteries and Interior-Permanent-Magnet (IPM) traction motor. The battery charger is integrated in the power hardware of the scooter, with the IPM traction drive that operates as three-phase dc-dc converter with Power Factor Correction (PFC) capability. The control of the PFC battery charger is also integrated into the traction control code that is performed by a fixed-point DSP controller. Current-controlled and voltage-controlled battery charge are actuated according to the requirements of the Battery Management System (BMS), that is embedded in the battery pack. Respect to other on-board chargers, the AC current is absorbed at unitary power factor with no harmonic distortion and no particular filtering is needed since the PWM ripple is minimized by interleaving the three phases of the converter. Other type of motors are also considered (IM, SMPM) and commented. The feasibility of the integral battery charger is demonstrated on a prototype electric scooter with high voltage battery (260V nominal).

I. INTRODUCTION

The traction battery is the most critical component of any electric vehicle: the cost, the weight, the driving range and the reliability of the vehicle are strongly influenced by the battery. The full exploitation of the battery capacity and the respect of the nominal lifetime are strongly influenced by the characteristics of the battery charger.

On-board battery chargers are appropriate for charging the battery by a source with limited power, like the single-phase household utility outlet. The weight and the volume of the charger must be minimized, since it must be carried by the vehicle. Battery current and voltage must be regulated according to the specifications of the manufacturer and according to the estimated state of charge. Last, the AC current supplied by the distribution system must respect the international standards of high power factor and low harmonics distortion [1].

The integral battery charger presented here uses the power conversion hardware of an electric scooter with very few additional components. Integral chargers have been proposed by different authors [2]–[4]. In particular, the idea of accessing the motor center tap to use the motor as a coupling inductor was first introduced in [3], for an electric car with 4 motor drives. A simpler conversion topology is proposed for an electric scooter in [4], where the center tap of the motor is connected to a rectifier via a mechanical switch, and the traction inverter is operated as a dc-dc boost battery charger. The same principle is applied here with significant improvements:

- the Power-Factor-Correction capability;
- the multi level approach by means of phase interleaving, that minimizes the PWM ripple and improves the control dynamics;
- the modeling of the IPM motor as a feasible coupling inductor;
- the investigation of charger integration with other type of motors (IM, SMPM).

The electric scooter under test is a prototype of big urban scooter (2 persons, 90km/h max), equipped with two Lithium-Ion battery packs (260V, 10Ah each). Detailed ratings are reported in the Appendix.

The paper is organized as follows. In section II, the power conversion structure of the electric scooter be described and the integrated battery charger will be presented. In section III the 4-wire model of the IPM motor drive will be developed in common-mode and differential-mode components. In section IV the 3-phase boost converter behavior will be described in detail and the analysis will be extended to other AC traction motors. In section V, the PFC control strategy will be outlined. In section VI the experimental results will be presented and commented.

II. POWER CONVERSION STRUCTURE.

The electric scooter powertrain is represented in Fig.1. It consists of the AC motor drive plus a DC/DC bidirectional stage. The evidenced *extra hardware components* are representative of the hardware that is needed for adapting the traction drive to the battery charger purpose: they are a single-phase rectifier bridge with a mechanical switch to access the center tap of the motor, a $3\mu F$ capacitor and an EMI filter. The measure of the rectified voltage (v_N) is also needed. All the other measures by the power charger are already available for the AC motor drive.

The 3-phase inverter operates here as an interleaved PFC boost rectifier with the IPM motor used as a coupled inductor. Multi-phase, interleaved converters with coupled inductors have been considered by many authors for their very low current ripple and high dynamics and are particularly suited for single phase PFC rectifiers [5], [6]. Respect to non-coupled

978-1-4244-4252-2/09/$25.00 ©2009 IEEE

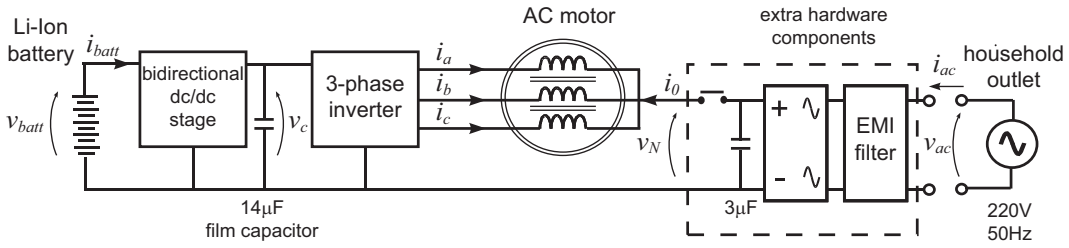

Fig. 1. Integrated battery charger: the traction drive is transformed into a 3-phase PFC boost battery charger.

reactors, these structures show higher control dynamics at given current ripple [7], [8].

The power absorbed from the single phase AC supply has a large $100Hz$ component that can not be accumulated by the dc-link film capacitor without reaching disruptive voltage levels (see Fig.1). For this reason, the DC/DC stage is used to regulate the dc-link voltage at a constant value ($330V$). Thus, the battery current presents a significant $100Hz$ component, whose effects will be discussed later. The DC/DC stage does not need a specific control algorithm for charge operation since its scope is to regulate the dc-link voltage also during traction time (the setpoint is $400V$ in motoring). The boost converter circuit is reported in Fig.2, where abc are the motor terminals and the phase currents represented in the motor notation. The neutral point N of the motor is the input terminal of the boost converter. The input current is indicated with i_0 it is the zero-sequence current of the IPM motor. The zero-sequence inductance L_0, put in evidence in Fig.2, is the input impedance of the boost converter. The input current is regulated by controlling the common-mode voltage of the inverter. The high side switches are not enabled: this gives practically no difference in terms of PFC performance and has a beneficial effect on the overall switching losses. Ideal switches and continuous current mode are considered here. The phase switching frequency is $20kHz$. The scope of sections IV and V will be to describe the operation of the interleaved boost operating at constant output voltage (V_c).

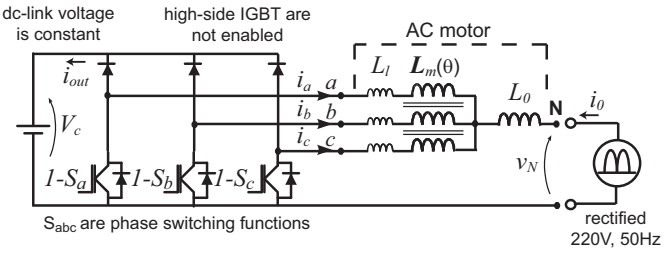

Fig. 2. Three-phase boost converter obtained by the IPM motor traction drive.

III. Model of the 4-wire IPM motor drive.

The state equation of the 4-wire motor drive is reported in (1).

$$\frac{d\lambda_{abc}}{dt} + R \cdot i_{abc} = S_{abc} \cdot V_c - v_N \tag{1}$$

Where λ_{abc} are the phase linked fluxes, S_{abc} are the phase switching functions of the inverter and R is the stator resistance. The notation X_{abc} is used for column vectors. The flux derivative (2) is related to the current derivatives by means of the three inductance terms evidenced in the schematics of Fig.2: the zero-sequence inductance $\mathbf{L}_0$ (3), that plays a key role in boost operation and it is due to 3-rd order magneto-motive-force (mmf) harmonics, the mutually-coupled inductances $\mathbf{L}_m$ (4) and the phase leakage inductances L_l. Due to the rotor saliency, the self and mutual inductances summarized of $\mathbf{L}_m$ depend on the rotor electrical position θ, as represented in Fig.3. The complete expression of phase inductances in terms of the L_{md}, L_{mq} synchronous inductances is reported in (5). The flux of the permanent magnets of the IPM motor gives no contribution since the motor is steady.

$$\frac{d\lambda_{abc}}{dt} = [L_l + \mathbf{L}_m(\theta) + \mathbf{L}_0] \cdot \frac{di_{abc}}{dt} \tag{2}$$

$$\mathbf{L}_0 = L_0 \cdot \begin{bmatrix} 1 & 1 & 1 \\ 1 & 1 & 1 \\ 1 & 1 & 1 \end{bmatrix} \tag{3}$$

$$\mathbf{L}_m(\theta) = \begin{bmatrix} L_{ma} & L_{mab} & L_{mca} \\ L_{mab} & L_{mb} & L_{mbc} \\ L_{mca} & L_{mbc} & L_{mc} \end{bmatrix} \tag{4}$$

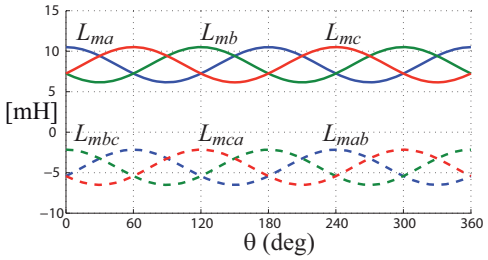

Fig. 3. Inductances of the IPM motor under test versus rotor electrical position θ. L_d = 6mH, L_q = 10.5mH.

A. Common-mode and differential-mode approach.

The adoption of common-mode and differential-mode models for multi phase systems has been proposed in [9]. In partic-

$$\mathbf{L}_m(\theta) = \frac{L_{md}+L_{mq}}{2}\cdot\begin{bmatrix} 1 & -\frac{1}{2} & -\frac{1}{2} \\ -\frac{1}{2} & 1 & -\frac{1}{2} \\ -\frac{1}{2} & -\frac{1}{2} & 1 \end{bmatrix} - \frac{L_{md}-L_{mq}}{2}\cdot cos(2\theta + \begin{bmatrix} 0 & -\frac{2\pi}{3} & +\frac{2\pi}{3} \\ -\frac{2\pi}{3} & +\frac{2\pi}{3} & 0 \\ +\frac{2\pi}{3} & 0 & -\frac{2\pi}{3} \end{bmatrix}) \tag{5}$$

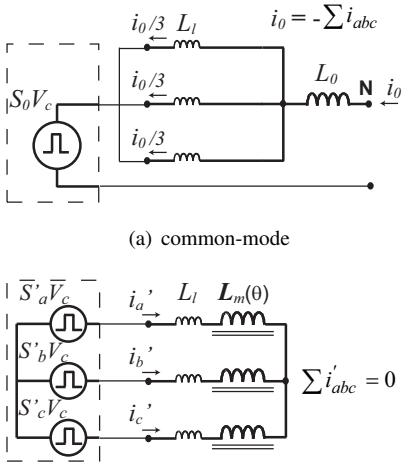

Fig. 4. Common-mode (boost operation) and differential-mode (3-wire motor) models of the IPM motor and of the inverter.

ular, it has been successfully adopted for n-phase boost converters in [10], where the common mode component controls the power flow of the converter, while $n-1$ differential-mode currents are controlled to zero for balanced current sharing. The transformation from phase to common and differential-mode currents adopted here is defined in (6),(7). It is a little bit unconventional due to the sign of the boost current that is opposite to motor convention. In the following, the phase differential-mode (dm) components will be indicated as abc with an apex, while the common-mode (cm) will be indicated with 0.

$$i_0 = -\sum i_{abc} \tag{6}$$

$$i_{abc} = i'_{abc} - i_0/3 \tag{7}$$

By manipulating the abc magnetic model (2) according to (6)-(7), the 0 (8) and dm (9) models are derived.

$$\lambda_0 = -\sum \lambda_{abc} = (L_l/3 + L_0)\cdot i_0 \tag{8}$$

$$\lambda'_{abc} = (L_l + \mathbf{L}_m(\theta))\cdot i'_{abc} \tag{9}$$

IV. 3-PHASE BOOST CONVERTER MODEL.

In Fig.4 the cm and dm components of the IPM motor are associated to the respective inverter voltage components to put in evidence the effectiveness of the proposed approach: the input current i_0 will be managed by means of the common-mode duty-cycle of the inverter, while the residual part of the motor currents, or dm, will be controlled to zero by means of the AC drive control for phase currents balancing.

The boost converter dynamics is described by the common-mode state equation (10), obtained from (1) and (8).

$$(L_l/3 + L_0)\cdot\frac{di_0}{dt} + R_s/3\cdot i_0 = v_N - V_c\cdot S_0 \tag{10}$$

The switching function S_0 defined in (11) represents the inverter common-mode voltage while the corresponding duty-cycle is the input to output voltage transfer ratio of the converter (12).

$$S_0 = \frac{\sum S_{abc}}{3} = \frac{(0,1,2,3)}{3} \tag{11}$$

$$D_0 = \int_0^{T_s} S_0\cdot dt \cong \frac{V_N}{V_c} \tag{12}$$

Where T_s is the phase switching period and the capital letters stand for the average values in T_s. The resistive drop has been neglected in the voltage ratio expression (12). The *boost equation* (10) is summarized in Fig.4-a. The four instantaneous values of S_0 stand for the multi-level capability of the boost converter. It is worthy to note that the rotor position does not appear in (10) since the $\mathbf{L}_m(\theta)$ matrix has no zero-sequence component: thus *it is demonstrated that the multi-level boost capability that can be obtained with balanced coupling inductors, like in [10], can also be obtained by means of a 3-phase motor having a salient rotor.*

A. Phase currents equalization.

The differential-mode state equation is obtained from (1) and (9).

$$(L_l + \mathbf{L}_m(\theta))\cdot\frac{di'_{abc}}{dt} + R\cdot i'_{abc} = S'_{abc}\cdot V_c \tag{13}$$

Where S'_{abc} are the differential-mode switching functions. As suggested by Fig.4-b, the differential-mode model is coincides with the 3-wire motor behavior and will be managed, for convenience, by means of the (d,q) synchronous components (14).

$$\begin{bmatrix} L_d & 0 \\ 0 & L_q \end{bmatrix}\cdot\frac{di_{dq}}{dt} + R\cdot i_{dq} = v_{dq} \tag{14}$$

Where $L_d = L_l + L_{md}, L_q = L_l + L_{mq}$. For having balanced phase currents, the d,q currents can be controlled to zero by means of the vector control of the IPM motor drive (15).

$$I_d = I_q = 0 \Rightarrow I_a = I_b = I_c \tag{15}$$

Where the capital letters indicate the average in the PWM period. Rhe dm currents will contribute only to phase current

ripple, since they have zero average value.

B. Phase interleaving and current ripple.

Phase interleaving means that the phase commands of the boost converter are regularly spaced respect to the switching period like in Fig.5 [11]. The following points must be remarked:

- the equivalent switching frequency of the input and output currents is three times the phase switching frequency ($20 \times 3 = 60kHz$ in this case);
- consequently, the input and output current ripple is strongly reduced and it is easier to filter;
- the input current ripple is zero for singular voltage transfer ratios ($v_N = 1/3, 2/3 \cdot V_c$ as in Fig.7);
- the differential-mode modulation produces a phase current ripple component at the fundamental PWM frequency ($20kHz$);
- the significant mutual coupling, limits the amplitude of the $20kHz$ ripple and improves the conversion efficiency and the control dynamics [7].
- with mutual coupling, the phase current ripple is limited by the large mutually coupled-inductances (L_{ma}, L_{mb}, L_{mc}) while the dynamics of i_0 is fast because it depends on the small inductance L_0 only.

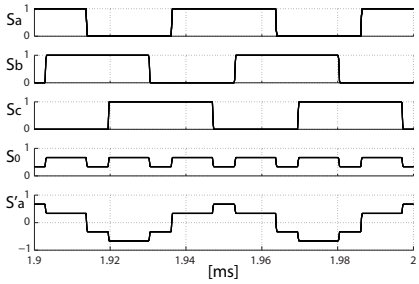

Fig. 5. Interleaved switching commands S_{abc} for $D_0 = 0.56$: S_0 is the common-mode switching function and S'_a is the differential-mode switching function of phase a.

For better clarity, the current waveforms of the interleaved converter are reported in Fig.8 for $5A$ input current, steady-state, in three different D_0 situations that produce the same input ripple. The steady-state amplitude of the i_0 ripple depends on the voltage transfer ratio D_0 as reported in Fig.7: the plot has been obtained by integrating (10) over one third of the switching period [10]. All the needed parameters are reported in the Appendix.

C. Effect of the rotor saliency on the ripple.

As demonstrated by equation (10), the rotor saliency have no effect on i_0. The only effect of saliency is that the differential-mode current ripple of the three phases will be different, according to the L_{ma}, L_{mb}, L_{mc} values outlined in (4) and in Fig.3. The dm ripple waveform of phase b (i'_b) has been reported in Fig.8 in different voltage transfer situations. As for the i_0 ripple, its amplitude depends on the D_0 transfer ratio. Apart for the waveform shape, the ripple amplitude is inversely proportional to the actual phase inductance: the two extreme situations are when one phase is aligned to the d

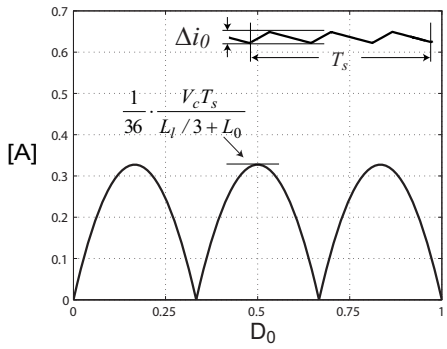

Fig. 7. Peak to peak amplitude of the input current ripple, that is at $60kHz$ and mainly depends on L_0.

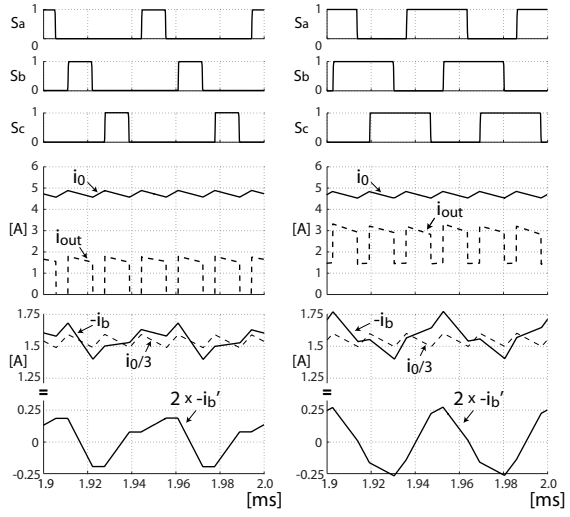

(a) $D_0 = 0.23$ (b) $D_0 = 0.56$

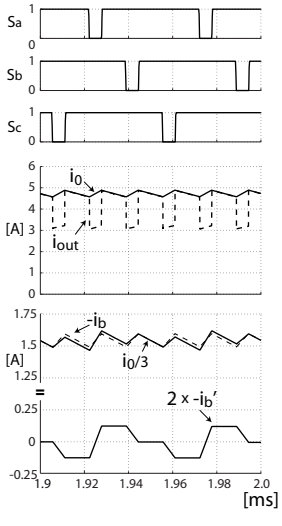

(c) $D_0 = 0.89$

Fig. 8. Steady-state current waveforms for different input/output voltages. The i_0 ripple is the same in three cases. The dm component of phase *b* current is evidenced (i'_b).

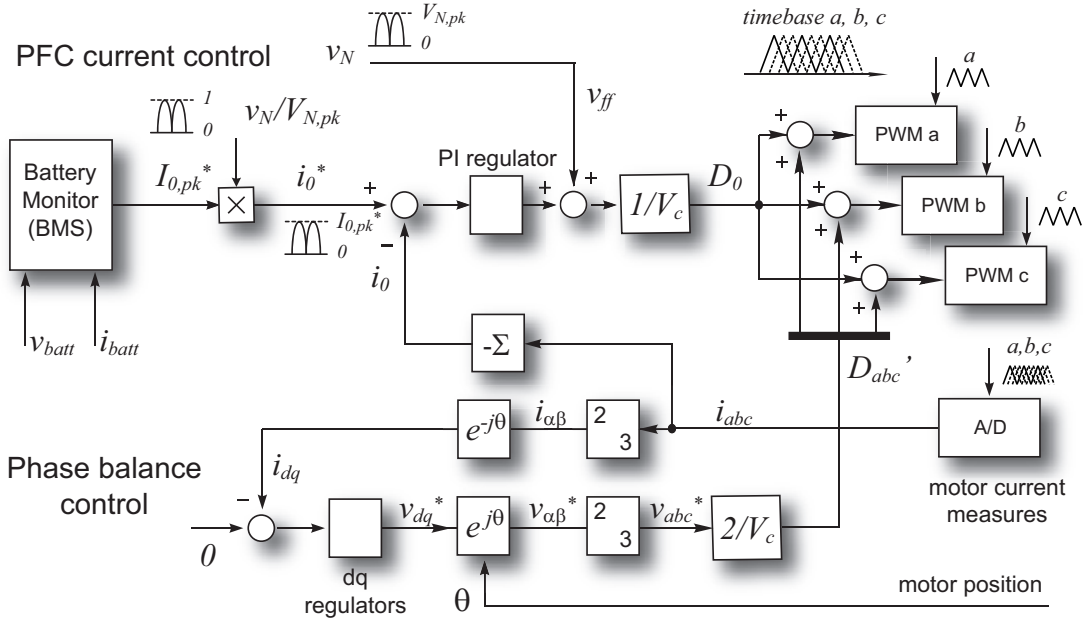

Fig. 6. Current control of the PFC boost battery charger with interleaved phases.

axis (maximum ripple amplitude) or to the q axis (minimum ripple amplitude). In Fig.9 the amplitude of the differential-mode ripple is reported as a function of D_0 for the prototype under test: the d (worst case) and q (best case) situations are reported. The plots of Fig.9 have been obtained by integration of (13) and considering (4). The needed drive parameters are in the Appendix.

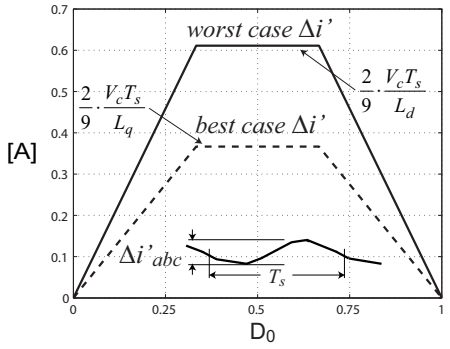

Fig. 9. Peak to peak amplitude of the differential-mode current ripple. The continuous line is the worst case situation (phase aligned to d), while the dashed line is the best case (phase aligned to q).

D. Feasibility with different motor types.

Different motor types can be considered for electric vehicles, namely Surface Mounted PM (SMPM) motors and IM motors [12].

Dealing with SMPM motors, the thick air-gap (air-gap plus magnet lenght) reduces both the zero-sequence and the phase inductances, thus a higher current ripple is expected both on the input and the phase currents (see Fig.7 and Fig.9). Due to low inductances, the dynamics is fast but the ripple produces large zones of discontinuous current operation than a difficult control of the PFC.

A particular case is represented by SMPM machines with concentrated windings, that show higher inductance values [13]. This contributes to have an acceptable current ripple, but still the PFC control dynamics suffers from the low mutual coupling due to the thick air-gap: the differential-mode inductance ($L_l + \mathbf{L}_m$ is high due to the non-coupled term L_l, but also the common-mode term ($L_l/3 + L_0$) is high due to L_l.

Dealing with Induction Motor drives (IM), the rotor cage reacts to the differential-mode stator currents, thus the mutual coupling of the stator phases is vanished by the rotor currents. The zero-sequence inductance is not affected by rotor reaction since the squirrel cage can not give zero-sequence currents. The result is a 3-phase inductor with no practical coupling where the differential-mode currents are limited only by the short-circuit inductances (stator + rotor leakage). The consequential high phase ripple suggests that all the inverter switches will be commanded (high side included), to avoid heavy discontinuous current mode and side effects on the PFC control. Lower efficiency and a bigger EMI filter are expected with an IM drive.

V. PFC CURRENT CONTROL.

The control scheme of the battery charger is reported in Fig.6. The unitary power factor at the AC side is obtained by the synchronization of the input current i_0 with the rectified AC voltage ($v_N = |v_{ac}|$). The measured quantities are the motor phase currents, the dc-link voltage and the input voltage v_N. Apart for the PWM ripple that is minimized by phase interleaving and filtered by the $3\mu H$ input capacitor and the EMI filter, the Total Harmonic Distortion (THD) factor

of the AC current relies on the performance of the current controller. The current amplitude set point I_0^* is provided by the Battery Management System (BMS) with a maximum of $8.5A$ (pk) that corresponds to $1300W$ maximum power absorbed from the household outlet. The BMS is embedded in the battery stack and it is capable of monitoring the voltage of all the elements in series in real time [14]. As introduced in section IV, the d, q current controller of the IPM motor drive guarantees the current sharing equalization. The PWM units have individual interleaved counters that are used for synchronization of the switching commands and of the motor currents sampling. In the presented prototype the control of all the scooter converters (double DC/DC plus 3-ph inverter) is managed by an industrial DSP (Freescale 56F801), while all the PWM and analog to digital functions are implemented on an FPGA. Nevertheless, many up-to-date DSP controllers can manage individual timebases for PWM and A/D sampling. The dc-link is controlled at $330V$ that is $20V$ higher than the AC mains peak so that the D_0 regulation range is fully exploited (from zero to 0.94, more or less).

A. Input current control.

The input current control scheme is reported in the upper part of Fig.6. The current reference shape is given by the rectified voltage v_N while the amplitude is given by the BMS. The current regulator is of the Proportional-Integral type. The feed-forward voltage term v_{ff} is strictly necessary to obtain a good tracking of the reference current, in particular around zero where the slope of i_0^* is discontinuous [15], [16]. As clearly explained in [15], the voltage controlled by the inverter ($D_0 \cdot V_c$) and then the optimal voltage feed-forward should reproduce the rectified voltage plus a load-dependent term due to the series inductance drop at $50Hz$ ($L_0 + L_l/3$ plus the EMI filter), thus v_{ff} should ideally be delayed respect to v_N in proportion with the load current. Once the feed-forward is correctly evaluated, the PI regulator compensates for second approximation errors and non-idealities. In practical implementation the following issues must be considered:

- the inductive drop at $50Hz$ is very low ($4Vpk$ with $8.5Apk$ line current) thus the time delay of the feed-forward is small also at maximum load ($40\mu s$ at maximum load).
- the DSP time-discretization introduces an actuation delay that practically coincides with the time delay required at full load.

For these reasons in the prototype the v_N measure is directly added in feed-forward, with no load-dependent delay ($v_{ff} = v_N$).

B. Current equalization by means of the $d-q$ control.

The d, q vector control of the IPM motor is used for the equalization of the phase currents with no modification, apart for the PWM synchronization that has been already discussed. The 3-phase to 2-phase transformation evidenced in the lower part of Fig.6 eliminates the zero current sequence thus the differential-mode duty cycles that are added to the D_0 reference are different from zero only in case of current unbalance.

VI. Experimental results.

The power board of the scooter is reported in Fig.10. The board size is $175mm \times 220mm$ and includes all the power converters of the scooter: the 3-phase inverter and two H-Bridge DC/DC stages, one per battery pack. The extra hardware components for battery charge operation are evidenced in the figure.

A preliminary set of tests regarded the evaluation of the high frequency inductances of the IPM motor performed by means of square wave excitation. The test conditions are the ones reported in Fig.12 In Fig.13 the zero-sequence inductance is evaluated at $20kHz$. The iron loss effect is evidenced by the current discontinuity and by the subsequent current transient. The inductance evaluated at $20kHz$ is $1.4mH$ while the apparent inductance at $60kHz$ can be significantly higher due to iron loss. In Fig.14 the differential-mode test is performed for different rotor alignments. The test is given at $1kHz$ for having the iron loss transient completely extinguished. Dealing with the q axis alignment the asymptotic inductance value corresponds to the low frequency L_q while the apparent inductance at $20kHz$ is significantly lower ($10mH$). The

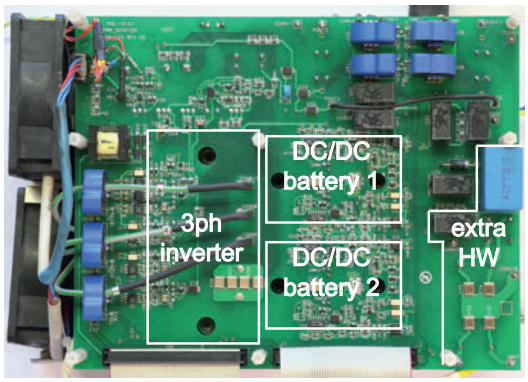

Fig. 10. Power board of the electric scooter: the extra hardware components of the battery charger are put in evidence. The size of the board is $175mm \times 220mm$.

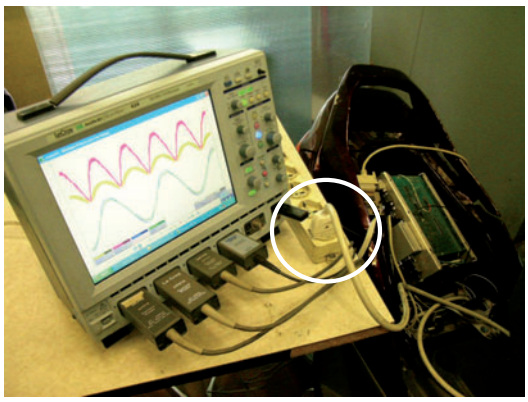

Fig. 11. Recharge of the scooter and measurement setup. The AC plug is evidenced in the circle.

L_d measure is practically not affected by iron loss effect. In Fig.14 the phase to neutral voltage is also reported: the asymptotic value is independent from the motor alignment, as demonstrated in (10), while the transient values are different in Fig.14(a) and (b) since the iron loss effect has not been considered in the proposed motor model.

The experimental setup for PFC performance tests is reported in Fig.11. The AC plug is evidenced. The i_0 and AC currents are reported for different motor alignments in Fig.16 and Fig.15. The good performance of the PFC control

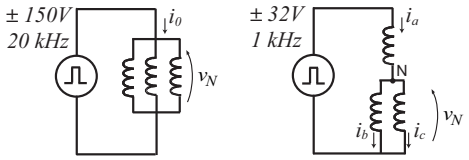

(a) cm (b) dm

Fig. 12. Square-wave tests for the evaluation of common-mode and differential-mode inductances.

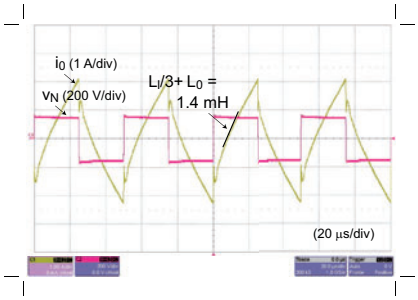

Fig. 13. Square wave test ($20kHz$) for the evaluation of the zero-sequence inductance.

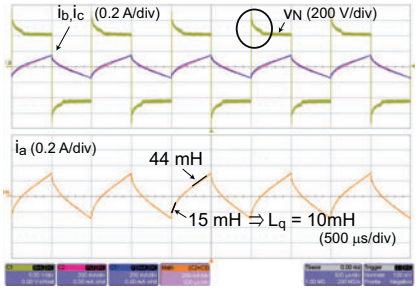

(a) d-axis

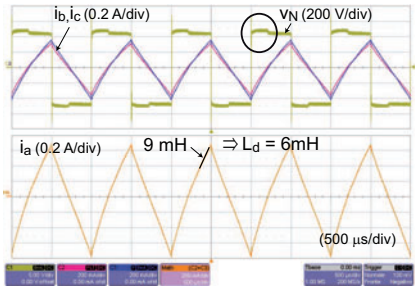

(b) q-axis

Fig. 14. Square wave test ($1kHz$) and evaluation of differential-mode L_d, L_q inductances at $20kHz$.

is demonstrated by comparison with the AC voltage. The perturbation around zero-crossing is due to the imperfect voltage feedforward implementation. The ripple of i_0 evidences the singular situations $D_0 = 1/3$ and $D_0 = 2/3$. The PWM ripple on the AC current is practically canceled. The current sharing is correct as demonstrated by the reported phase current. The phase ripple is minimum in Fig.15 (phase aligned with the q axis) and maximum in Fig.16 (phase aligned with the d axis) but no particular effect is noticed with different alignments.

In Fig.17 the current of one of the battery packs is reported. The superimposed modulation ripple is at $20kHz$ and it is due to the DC/DC stage the regulates the dc-link voltage. The ripple has a constant amplitude since the battery to dc-link voltage ratio is constant and the DC/DC works at constant duty-cycle. The consequences of non-steady charge current on battery life and performance are still under investigation and are also different for different battery technologies. No significant side effects have been outlined so far in the prototype and in the literature [17], [18].

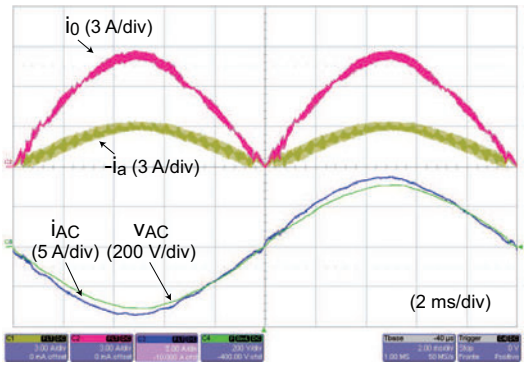

Fig. 15. PFC charge operation: the represented phase is aligned with the d axis, that is the minimum ripple situation.

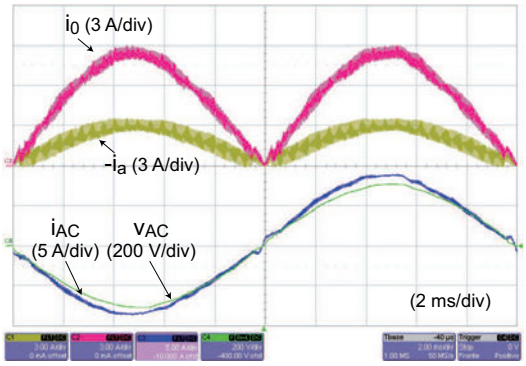

Fig. 16. PFC charge operation: the represented phase is aligned with the q axis, that is the maximum ripple situation.

VII. Conclusions

An integral battery charger has been proposed and experimentally tested for an electric scooter with Li-Ion batteries and IPM traction motor. The multi-level boost converter with PFC capability is obtained by the IPM motor drive with few

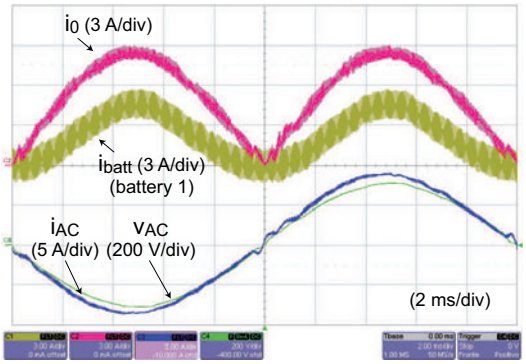

Fig. 17. Battery current with $100Hz$ component. The PWM ripple is due to the DC/DC stage.

additional components. The charger control is integrated into the control code of the scooter, that is performed by a fixed-point DSP controller. The analysis and the experimental results show that the IPM motor can be successfully adopted as a coupling inductor, that the rotor saliency gives no practical side effect and that the AC current is absorbed at unitary power factor with very limited distortion with no additional passive filtering apart for a standard EMI filter. Induction and SMPM motors have been also analyzed and lower performance are expected respect to IPM motor. The battery current has a significant $100Hz$ component, whose consequences are still under discussion in the literature.

APPENDIX: SCOOTER PROTOTYPE RATINGS

TABLE I
SCOOTER PROTOTYPE RATINGS.

	Scooter	
Total weight	incl. 2 passengers	$320kg$
Max Speed		$90km/h$
Driving range	$@50km/h$	$130km$
Traction Power (peak)		$10kW$
	Batteries (2 packs)	
Voltage	nominal	$260V$
Current	maximum	$2 \times 30A$
Weight		$2 \times 24kg$
Capacity		$2 \times 10Ah$
	IPM motor drive	
Rated, max speed		$2500, 10000rpm$
Back-EMF	$10000rpm$, phase	$145Vpk$
L_d, L_q	unsat, nominal	$6mH, 40mH$
L_d, L_q	$@20kHz$	$6mH, 10mH$
$L_0(+L_l/3)$	$@20kHz$	$1.4mH$
PWM frequency	$1/T_s$	$20kHz$
dc-link voltage	traction	$400V$
dc-link voltage	charge	$330V$

REFERENCES

[1] J. Carlos Gomez and Medhat M. Morcos. Impact of ev battery chargers on the power quality of distribution systems. *IEEE TRANSACTIONS ON POWER DELIVERY*, 18(3):975 – 981, 2003.

[2] David Thimmesch. An scr inverter with an integral battery charger for electric vehicles. *Industry Applications, IEEE Transactions on*, IA-21(4):1023–1029, July 1985.

[3] Seung-Ki Sul and Sang-Joon Lee. An integral battery charger for four-wheel drive electric vehicle. *Industry Applications, IEEE Transactions on*, 31(5):1096–1099, Sep/Oct 1995.

[4] L. Solero. Nonconventional on-board charger for electric vehicle propulsion batteries. *IEEE TRANSACTIONS ON VEHICULAR TECHNOLOGY*, 50(1):144 – 149, 2001.

[5] R. Redl and L. Balogh. Power-factor correction in bridge and voltage-doubler rectifier circuits with inductors and capacitors. *Applied Power Electronics Conference and Exposition, 1995. APEC '95. Conference Proceedings 1995., Tenth Annual*, (0):466–472 vol.1, Mar 1995.

[6] J. Salmon, A. Knight, J. Ewanchuk, and N. Noor. Multi-level single phase boost rectifiers using coupled inductors. *Power Electronics Specialists Conference, 2008. PESC 2008. IEEE*, pages 3156–3163, June 2008.

[7] Pit-Leong Wong, Peng Xu, P. Yang, and F.C. Lee. Performance improvements of interleaving vrms with coupling inductors. *Power Electronics, IEEE Transactions on*, 16(4):499–507, Jul 2001.

[8] Wei Wen and Yim-Shu Lee. A two-channel interleaved boost converter with reduced core loss and copper loss. *Power Electronics Specialists Conference, 2004. PESC 04. 2004 IEEE 35th Annual*, 2:1003–1009 Vol.2, June 2004.

[9] A. Garg, D.J. Perreault, and G.C. Verghese. Feedback control of paralleled symmetric systems, with applications to nonlinear dynamics of paralleled power converters. *Circuits and Systems, 1999. ISCAS '99. Proceedings of the 1999 IEEE International Symposium on*, 5:192–197 vol.5, 1999.

[10] H.-B. Shin, J.-G. Park, S.-K. Chung, H.-W. Lee, and T.A. Lipo. Generalised steady-state analysis of multiphase interleaved boost converter with coupled inductors. *Electric Power Applications, IEE Proceedings* -, 152(3):584–594, May 2005.

[11] D.J. Perreault and J.G. Kassakian. Distributed interleaving of paralleled power converters. *Circuits and Systems I: Fundamental Theory and Applications, IEEE Transactions on*, 44(8):728–734, Aug 1997.

[12] Gaurav Nanda and Narayan C. Kar. A survey and comparison of characteristics of motor drives used in electric vehicles. *Electrical and Computer Engineering, 2006. CCECE '06. Canadian Conference on*, pages 811–814, May 2006.

[13] A.M. EL-Refaie and T.M. Jahns. Optimal flux weakening in surface pm machines using fractional-slot concentrated windings. *Industry Applications, IEEE Transactions on*, 41(3):790–800, May-June 2005.

[14] A. Affanni, A. Bellini, G. Franceschini, P. Guglielmi, and C. Tassoni. Battery choice and management for new-generation electric vehicles. *Industrial Electronics, IEEE Transactions on*, 52(5):1343–1349, Oct. 2005.

[15] D.M. Van de Sype, Koen De Gusseme, A.P.M. Van den Bossche, and J.A. Melkebeek. Duty-ratio feedforward for digitally controlled boost pfc converters. *Industrial Electronics, IEEE Transactions on*, 52(1):108–115, Feb. 2005.

[16] Hung-Chi Chen and Chih-Kai Huang. Phase feedforward control for single-phase boost-type smr. *Applied Power Electronics Conference and Exposition, 2008. APEC 2008. Twenty-Third Annual IEEE*, pages 1313–1318, Feb. 2008.

[17] F. Lacressonniere, B. Cassoret, and J.-F. Brudny. Influence of a charging current with a sinusoidal perturbation on the performance of a lead-acid battery. *Electric Power Applications, IEE Proceedings* -, 152(5):1365–1370, Sept. 2005.

[18] J. Li, E. Murphy, J. Winnick, and P.A. Kohl. The effects of pulse charging on cycling characteristics of commercial lithium-ion batteries. *Journal of Power Sources*, 102:302–309, 2001.

[19] T. Matsuo and T.A. Lipo. Rotor position detection scheme for synchronous reluctance motor based on current measurements. *Industry Applications, IEEE Transactions on*, 31(4):860–868, Jul/Aug 1995.